

# DRWKV: Focusing on Object Edges for Low-Light Image Enhancement

Xuecheng Bai<sup>1\*</sup> Yuxiang Wang<sup>2\*</sup> Boyu Hu<sup>3</sup> Qinyuan Jie<sup>1</sup>  
 Chuanzhi Xu<sup>2†</sup> Kechen Li<sup>4</sup> Hongru Xiao<sup>5</sup> Vera Chung<sup>2</sup>

## Abstract

Low-Light Image Enhancement (LLIE) remains a challenging task, particularly in preserving object edge continuity and fine structural details under extreme illumination degradation. In this paper, we propose a novel model, DRWKV (Detailed Receptance Weighted Key Value), which integrates our proposed Global Edge Retinex (GER) theory, enabling effective decoupling of illumination and edge structures for enhanced edge fidelity. Secondly, we introduce Evolving WKV Attention, a spiral-scanning mechanism that captures spatial edge continuity and models irregular structures more effectively. Thirdly, we design the Bilateral Spectrum Aligner Block (Bi-SAB) and a tailored  $MS^2$ -Loss to jointly align luminance and chrominance features, improving visual naturalness and mitigating artifacts. Extensive experiments on five LLIE benchmarks demonstrate that DRWKV achieves leading performance in PSNR, SSIM, and NIQE while maintaining low computational complexity. Furthermore, DRWKV enhances downstream performance in low-light multi-object tracking tasks, validating its generalization capabilities. The code are available at: <https://github.com/JackBaixue/DRWKV>

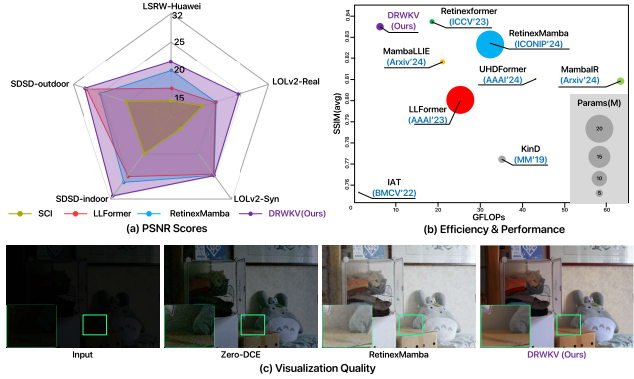


Figure 1. Comparison of our DRWKV with different methods: (a) DRWKV achieves the best PSNR in benchmark tests; (b) DRWKV balances efficiency, parameters, and computational load; (c) DRWKV exhibits more robust performance in edge details.

where  $R$  denotes scene reflectance,  $L$  represents the illumination component, and  $N$  stands for intrinsic noise.

When constructing a low-light scene, for the image, in addition to the increase in noise  $N$ , the illumination component  $L$  is decomposed into global and local illumination. The global spectrum and contour light field will dynamically change under light reflection. In the context of low-light image quality improvement, focusing solely on global illumination will amplify background noise [36] and cause edge distortion [45], while focusing only on contours in isolation leads to rigid edge transitions. Therefore, under the condition that global exposure is controllable, the essence of low-light image enhancement lies in the refinement of object edges. As shown in Figure 1(c), ZeroDCE [12] suffers from edge distortion, and RetinexMamba [2] exhibits detail blurring, indicating that current methods have limitations in handling extremely low-light environments.

To address these issues, we propose **Detailed Receptance Weighted Key Value (DRWKV)** model, which optimizes the Bi-WKV Attention of VRWKV (in ICLR 2025) [10]—a classic model in the visual RWKV domain. We introduce the **Evolving WKV Attention**, a novel attention mechanism with superior spatial topological awareness, which can maximize the capture of continuous

## 1. Introduction

Low-Light Image Enhancement (LLIE) technology is regarded as an active method to brighten low-light images at low cost [30, 37]. Recently, the academic community has primarily explored prominent methods such as global attention modeling [35, 43, 48], local feature enhancement [12, 14, 51], and selective state updating [33, 56]. Based on the robust Retinex theory [20], the composition of a low-light image  $I$  can be interpreted as:

$$I = R \cdot L + N, \quad (1)$$

\*Equal contribution.

†Corresponding author: Chuanzhi Xu (chuanzhi.xu@sydney.edu.au).

### Affiliations:

<sup>1</sup>Shenyang Ligong University, Shenyang, China

<sup>2</sup>The University of Sydney, NSW, Australia

<sup>3</sup>University of International Business and Economics, Beijing, China

<sup>4</sup>Nanjing University of Aeronautics and Astronautics, Nanjing, China

<sup>5</sup>Tongji University, Shanghai, China

spatial information of object edges, thereby strengthening the modeling effect of irregular spatial structures. Following this, we design an auxiliary technique—**Bilateral Spectrum Aligner Block (Bi-SAB)**. By aligning brightness and color spectral features, Bi-SAB resolves issues of over-exposure and color distortion caused by separate processing. Coupled with **MS<sup>2</sup>-Loss**, Bi-SAB renders the illumination and colors of enhanced images more natural. We conducted extensive image-enhancement and low-light object-tracking experiments on five benchmark datasets. As illustrated in Figure 1(a) and 1(b), our method achieves leading PSNR, SSIM, and NIQE scores, demonstrating significant superiority in edge continuity and detail fidelity.

Our contributions can be summarized as follows:

- We propose **Detailed Receptance Weighted Key Value (DRWKV)** model, for the first time, integrating our proposed **Global Edge Retinex (GER)** theory with the VRWKV model. It effectively enhances the edge of the low-light image.
- We design a novel **Evolving Scanning (ES) mechanism** applied to WKV Attention, also namely **Evolving WKV Attention**. It mines edge details from the inside out, enhancing DRWKV’s in modeling irregular spatial structures of edges.
- We introduce **Bilateral Spectrum Aligner Block (Bi-SAB)**, which enriches the color domain of brightened low-light images by coordinating spectral features and coupling with our proposed **MS<sup>2</sup>-Loss**.

## 2. Related Work

### 2.1. Object Edge Perception and Extraction

Edge perception and extraction techniques are built upon traditional methods [6, 21, 25, 50] and deep learning approaches [12, 40]. They achieve fine-grained restoration of object edges in low-light scenarios by fusing decoupled edge features with contextual information.

Different from traditional CNN-based methods such as Retinex-Net [46] and LLNet [23] that rely on local convolutions to extract edge features, emerging edge-aware approaches introduce topological modeling [19, 38, 54]. These methods treat edges as “spatial sequences” and capture cross-regional features through state accumulation. This design offers a core advantage in enhancing weak edge signals by achieving balanced transitions and local optimization through the adjustment of edge gradient consistency constraints and dynamic thresholds.

### 2.2. Low-Light Object Edge Restoration and Enhancement

Previous efforts to improve object edge accuracy in complex low-light environments primarily focus on two direc-

tions: exploration of diverse model architectures and optimization of edge enhancement algorithms.

Techniques such as EDTER [31] and Retinex-RAWMamba [7] explore diverse architectures by leveraging self-attention to capture cross-regional dependencies and linear scanning to optimize temporal accumulation.

Robust edge extraction is achieved through frequency-domain feature filtering [11], multi-modal edge complementarity [22, 32], and adversarial learning-based edge constraints [2], further precisely enhancing edge features.

Despite these advances, the modeling of object edge consistency under the visual RWKV framework has received limited attention, particularly in complex low-light scenarios. This suggests a promising direction for integrating edge-aware fidelity modeling into RWKV-based architectures.

## 3. Methodology

**Rethinking Edge Fidelity Modeling in VRWKV:** The core of edge fidelity lies in strong consistency between structure and features. The limitations of VRWKV in low-light scenarios are analyzed from two aspects:

(1) *Neural Architecture.* VRWKV adopts a single recursive structure, which mismatches the hierarchical features of edges. This causes aliasing of shallow and deep features, manifested as the failure to decouple illumination variations from edge representation, and leads to frequent misjudgment between noise and edges in low-light environments.

(2) *Computational Geometry.* Edges are low-dimensional manifolds in high-dimensional pixel spaces, becoming more curved under low light due to drastic illumination fluctuations. However, VRWKV assumes features are uniformly distributed in Euclidean space, while edge manifolds actually reside in curved Riemannian spaces. This results in inaccurate Euclidean distance metrics (causing misclassification of edge features) and mismatching between the translation invariance of convolutions and edge scale variations under low light.

**Based on the results of our reasoning, we propose two hypotheses:** (1) Hierarchical detail enhancement depends on a gradient-guided mechanism with illumination invariance. (2) Modeling the continuity of low-light edges requires a spatiotemporal alignment modeling scheme compatible with the topological properties of edges.

**DRWKV Model:** Different from current mainstream methods, model adopts a layered optimization strategy, which prioritizes combining the gray-world assumption with a three-branch channel consisting of noise  $N$ , artifact  $S$ , and illumination  $L$  to implement (3.1) Light Preprocessing (LP), thereby obtaining the brightness-restored image  $\hat{I}$  [4]. For the Deep Detail Mining (DDM) process, the RWKV structure comprises a set formed by four groups of ES-RWKV and sampling blocks. For the encoder, (3.2)

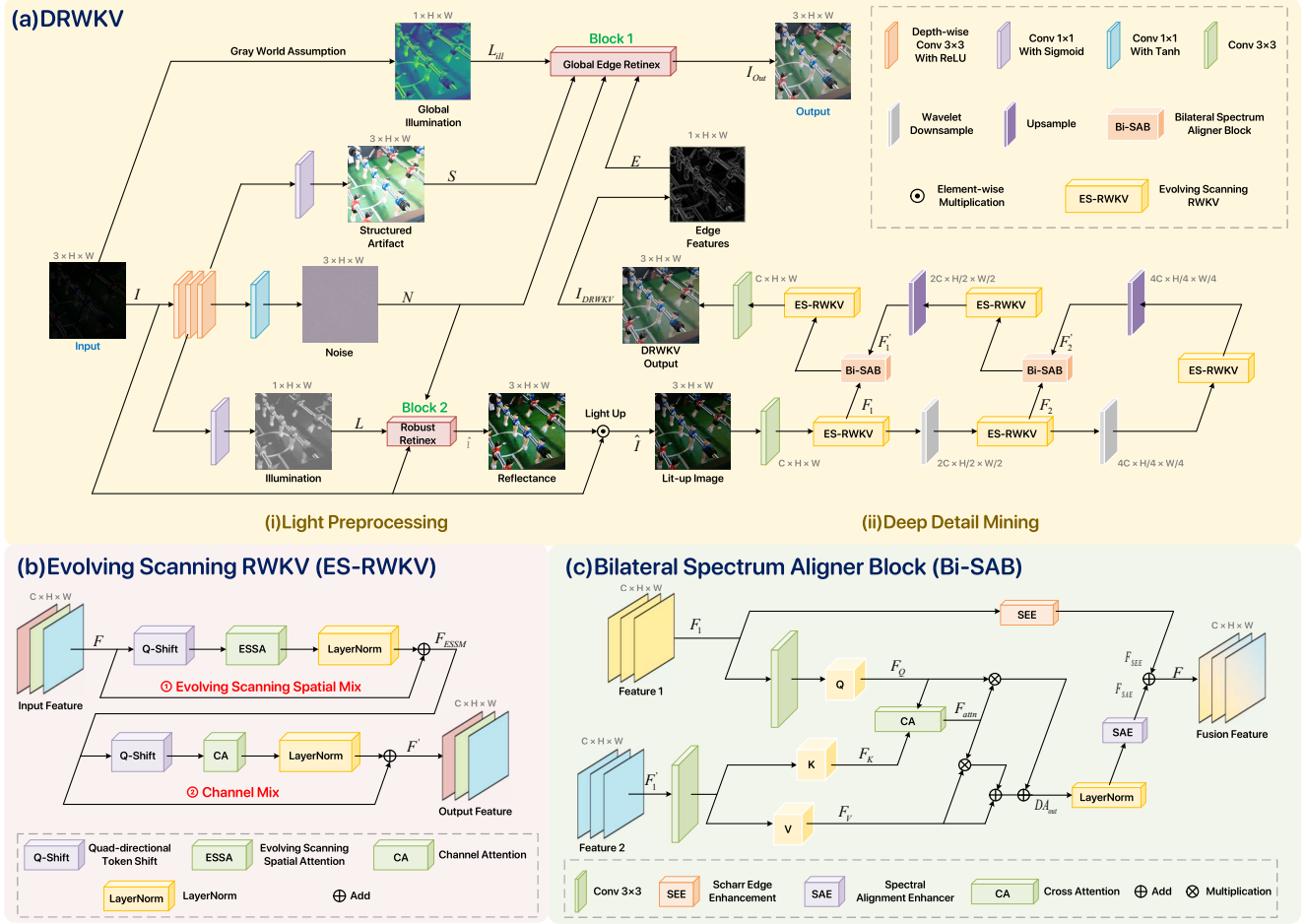


Figure 2. The overview of the DRWKV model. (a) DRWKV processes low-light images through two steps: (i) Light Preprocessing and (ii) Deep Detail Mining. The positions of Block1 and Block2 correspond to the layout settings of the two Retinex theories. (b) The block structure of Evolving Scanning RWKV, which embeds two core mixing modules: Evolving Scanning Spatial Mix and Channel Mix. (c) The block structure of the Bilateral Spectrum Aligner Block.

Evolving Scanning mechanism is applied for the first time, combined with wavelet transform downsampling to accomplish edge gradient feature extraction. The decoder integrates the sampling information  $F$  and  $F'$  via the (3.3) Bilateral Spectrum Aligner Block (Bi-SAB), enabling progressive enhancement from microscopic textures to macroscopic contours. The overall structure of our DRWKV model is provided in Figure 2.

### 3.1. Light Preprocessing

The Light Preprocessing (LP) structure employs a dual-path parallel guidance approach, balancing brightness, preserving details, and ensuring the baseline quality of LLIE results for the subsequent Deep Detail Mining (DDM) process. Technically, we recalculate the RGB components us-

ing the gray-world assumption  $L_{ill}$ :

$$L_{ill} = [R' \ G' \ B'] = \text{diag} \left( \frac{\frac{1}{3} \sum_{i=1}^N |c_i|}{\sum_{i=1}^N c_i} \right) \cdot c, \quad (2)$$

where  $c_i = [R_i, G_i, B_i]^T$  restructures the three-channel vector of a pixel. The detailed procedure involves converting the vector into a diagonal matrix via  $\text{diag}(\cdot)$  and then computing the inner product with the original channel vector  $c$ . By combining  $L_{ill}$  with the artifact component  $S$ , we explicitly define the interference boundaries to be avoided, enabling the Global Edge Retinex (GER) to enhance brightness without amplifying artifacts, thus achieving the first path of clean baseline enhancement.

We recognize that separating image information into an illumination component  $L$  and a noise component  $N$  allows for a more refined representation:

$$\hat{I} = I \times \hat{R} = I \times (I - N)/L. \quad (3)$$

In the second path, we process different information components by computing the product of the reconstructed reflectance component  $\hat{R}$  and the input low-light image  $I$ , resulting in a low-light enhanced image  $\hat{I}$  that retains the original detail information. Its for the subsequent RWKV stage.

### 3.2. Deep Detail Mining

#### Global Edge Retinex Theory

The traditional Robust Retinex theory has limitations in component decoupling and deep/shallow detail processing. Based on the hierarchical detail enhancement approach in *Hypothesis(1)*, we propose the Global Edge Retinex (GER) theory, and the core formula is as follows:

$$I = (R + \alpha \cdot E) \odot L_{ill} + \beta \cdot N + \gamma \cdot S. \quad (4)$$

The theory takes the explicit edge feature  $E$  (the formula is provided in Appendix 3.3), the spatially heterogeneous noise  $N$  (obtained after segmenting traditional noise), the gray-world assumption  $L_{ill}$ , the artifact  $S$ , and the learnable parameters  $\alpha, \beta, \gamma$  (which control feature expression) as the anchors for addressing low-light edge detail issues.

The specific breakdown is as follows: Deep edge structures exhibit illumination invariance, so GER uses the reflectance component  $R$  as the stable base:

$$R = \frac{I - N}{L_{ill} + \epsilon} \in [0, 1], \quad (5)$$

where  $R$  strips off spatially heterogeneous noise via  $I - N$  and neutralizes illumination interference through  $L_{ill} + \epsilon$ , providing a "clean" benchmark for detail enhancement.

From the model perspective, the edge feature  $E$  (processed by spiral gradient scanning) is used to construct the enhanced reflectance map:

$$R_{enh} = R + \alpha \cdot E. \quad (6)$$

The parameter  $\alpha$  is used to control the intensity of differential enhancement of deep/shallow details guided by  $E$ , ensuring clear feature hierarchy. Meanwhile, gradient information is incorporated to enhance edge continuity.

Finally, an enhanced image with edge fidelity is obtained through the collaborative balance of all components:

$$\hat{I} = R_{enh} \times L_{ill} + \beta \cdot N + \gamma \cdot S. \quad (7)$$

#### Evolving Scanning Mechanism

Evolving Scanning (ES) mechanism addresses *Hypothesis(2)* by transforming the geometric continuity of edge

manifolds into temporal continuity capturable by the VRWKV propagation mechanism. Its mathematical foundation lies in the Archimedean spiral equation:

$$P(\theta) = (r(\theta) \cos \theta, r(\theta) \sin \theta), \quad (8)$$

where  $r(\theta) = a + b\theta$  governs the initial radius ( $a$ ) and expansion rate ( $b$ ) of the spiral. The path expands uniformly from the starting point, naturally adapting to the edge characteristics of spreading from local to global regions. In terms of the scanning mechanism, we extend a single spiral to a four-directional rectangular spiral system. Let  $P$  denote the spiral path spreading outward from the center, and let  $P_i = (x_i, y_i)$  represent the coordinates of the  $i$ -th step (where  $i \in \mathbb{N}$ ). The coordinates satisfy:

$$P_i = (x_0, y_0) + (r_0 + \alpha \lfloor i/4 \rfloor) \cdot \delta_{i \bmod 4}, \quad (9)$$

where  $\delta \in \{(0, -1), (1, 0), (0, 1), (-1, 0)\}$ .

Here,  $(x_0, y_0)$  is the spiral center,  $r_0 > 0$  is the initial radius, and  $\alpha > 0$  is the radial pitch. The direction vector  $\delta_{i \bmod 4}$  cycles incrementally in the four directions of up, right, down, and left.

In terms of implementation, the spiral path is encoded into several token streams, which are input into the BiWKV attention mechanism for iterative modeling. By applying the proposed Evolving Scanning mechanism to the RWKV structure, we ultimately bridge the gap between the Riemannian manifold properties of low-illumination edges and the temporal modeling capability of RWKV. This significantly improves edge continuity and structural fidelity under low-light conditions (the formula derivation process is provided in Appendix 2):

$$ES\text{-}RWKV(\cdot) = \cdot + \mathcal{F}_{\text{spatial}}(\cdot) + \mathcal{F}_{\text{channel}}(F_{\text{ESSM}}), \quad (10)$$

where  $\cdot$  denotes the input feature,  $\mathcal{F}_{\text{spatial}}(\cdot)$  represents the spatial dependency modeling implemented via spiral scanning and the ES-RWKV mechanism, and  $\mathcal{F}_{\text{channel}}(\cdot)$  denotes the channel correlation modeling based on Q-Shift and nonlinear mapping.

### 3.3. Bilateral Spectrum Aligner Block

Edge detail optimization can ensure feature focusing in low-light images, but its optimization degree and feature matching degree are particularly crucial. Specifically, excessive emphasis on details will lead to the prominence of noise in low-light regions and the generation of artifacts. Mismatch with brightness and color features will degrade visual perception. To address this issue, the spectral alignment technique proposed by us is embedded into DRWKV in the form of a Bilateral Spectrum Aligner Block (BiSAB).

---

**Algorithm 1** Bi-SAB: Bilateral Spectrum Aligner Block

---

**Input:** Low-level Feature  $F_1$ :  $(B, C_i, H_i, W_i)$   
High-level Feature  $F_1'$ :  $(B, C_i, H_i, W_i)$   
**Output:** Bi-SAB Fusion Feature  $F$ :  $(B, C_i, H_i, W_i)$   
*/\*NOTE: Technical details are provided in the supplementary material.\*/*

- 1: */\*Compute the query (Q), key (K), and value (V) representations.\*/*
- 2:  $F_Q : (B, C_i, H_i, W_i) \leftarrow \text{Conv}_{3 \times 3}(F_1)$
- 3:  $F_K : (B, C_i, H_i, W_i) \leftarrow \text{Conv}_{3 \times 3}(F_1')$
- 4:  $F_V : (B, C_1, H_i, W_i) \leftarrow \text{Conv}_{3 \times 3}(F_1)$
- 5: */\*Compute Cross Attention (CA) feature representations.\*/*
- 6:  $F_{\text{attn}} : (B, C_1, H_i, W_i) \leftarrow \text{CA}(F_Q, F_K)$
- 7: */\*Compute Feature Difference Adjustment (FDA) feature representations.\*/*
- 8:  $\text{Att}_{\text{out}} : (B, C_1, H_i, W_i) \leftarrow F_{\text{attn}} \times F_K$
- 9:  $F_{\text{out}} : (B, C_1, H_i, W_i) \leftarrow \rho \cdot \text{Att}_{\text{out}} + F_V, \rho = 0.2$
- 10:  $F_{\text{DA}} : (B, C_1, H_i, W_i) \leftarrow F_{\text{attn}} \times F_Q + F_{\text{out}}$
- 11: */\*Compute Scharr Edge Enhancement (SEE) feature representations.\*/*
- 12:  $F_{\text{SEE}} : (B, C_i, H_i, W_i) \leftarrow \text{SEE}(F_1)$
- 13: */\*Compute Spectral Alignment Enhancer (SAE) feature representations.\*/*
- 14:  $F_{\text{SAE}} : (B, C_1, H_i, W_i) \leftarrow \text{SAE}(\text{LN}(F_{\text{DA}}))$
- 15: */\*Compute Bi-SAB feature representations.\*/*
- 16:  $F : (B, C_1, H_i, W_i) \leftarrow F_{\text{SAE}} + F_{\text{SEE}}$
- 17: **return**  $F$

---

Structurally, Bi-SAB enables feature interaction between the brightness and color branches through CrossAttention. It utilizes Spectral Alignment Enhancer (SAE) to enhance image brightness and reduce noise, and extracts edge details with the Scharr operator. The complete structural block provides feasible solutions for issues related to brightness, color, details, and noise. The specific process is shown in Algorithm 1.

### 3.4. Loss Function

The newly defined MS<sup>2</sup>-Loss focuses on five key attributes of the model: structure, edge, illumination, artifact, and weight.

**Decompositional consistency loss:** Inspired by compressed sensing theory [16], it applies the L1 norm to image reconstruction:

$$\mathcal{L}_{\text{recon}} = \|I - \hat{I}\|_1, \quad (11)$$

where  $\|\cdot\|_p$  denotes the  $p$ -norm.  $\mathcal{L}_{\text{recon}}$  focuses on balancing pixel-level errors and structural information.

**Edge sparsity loss:** The L1 loss is used to control the sparsity of edge contours and suppress false edges caused by noise:

$$\mathcal{L}_{\text{sparse}} = \|E\|_1, \quad (12)$$

Herein, the edge map  $E$  is non-zero only at real contours, while it should approach 0 at other positions, satisfying the sparsity prior condition.

**Illumination smoothness loss:** In natural scenes, illumination  $L$  exhibits characteristics of spatial smoothness and abrupt edge changes, requiring targeted handling:

$$\mathcal{L}_{\text{smooth}} = |\nabla L| \cdot \exp(-\lambda|\nabla I|), \quad (13)$$

where  $\nabla L$  is the illumination gradient, and  $|\nabla I|$  represents the image region. A high  $|\nabla I|$  indicates an edge region, where constraints on  $L$  should be relaxed to emphasize illumination naturalness; a low  $|\nabla I|$  indicates a flat region, where drastic changes in  $L$  are penalized to avoid invalid fluctuations in illumination.

**Artifact suppression loss:** A selection-regularized artifact suppression loss is proposed to minimize artifact energy and ensure spatial smoothness:

$$\mathcal{L}_{\text{artifact}} = \|S\|_1 + \delta \cdot \text{TV}(S), \quad (14)$$

where  $\delta$  is a weight parameter. When  $\delta > 1$ ,  $\mathcal{L}_{\text{noise}}$  is dominated by the TV regularization term, suppressing high-frequency oscillations such as halos and stripes; when  $\delta < 1$ , the loss is dominated by the L1 regularization term, controlling the magnitude of residuals.

**Parameter regularization loss:** Focusing on the optimization of learnable parameters  $\alpha$ ,  $\beta$ , and  $\gamma$ , L2 regularization is equivalent to weight decay, forcing parameter values to approach 0, with the formula as follows:

$$\mathcal{L}_{\text{reg}} = \alpha^2 + \beta^2 + \gamma^2. \quad (15)$$

**Total loss structure:** The total loss structure is given by

$$\begin{aligned} \mathcal{L}_{\text{MS}^2\text{-Loss}} = & \lambda_1 \mathcal{L}_{\text{recon}} + \lambda_2 \mathcal{L}_{\text{sparse}} + \lambda_3 \mathcal{L}_{\text{smooth}} \\ & + \lambda_4 \mathcal{L}_{\text{artifact}} + \lambda_5 \mathcal{L}_{\text{reg}}, \end{aligned} \quad (16)$$

where  $\lambda_i$  are predefined weights.

## 4. Experiments

### 4.1. Experimental Settings

**Implementation details:** We implement model training and inference on the NVIDIA A800-80GB platform. Specific parameter settings are as follows: the number of training epochs  $E$  is set to 500; the input image size  $S$  is 128×128; the block numbers of the DRWKV structure are set to  $N_1 = 4$  and  $N_2 = 8$  respectively, and the input channel number  $C$  is 16. The model optimizer uses Adam [17] with parameters set to  $\beta_1 = 0.9$  and  $\beta_2 = 0.999$ ; the initial learning rate is  $2 \times 10^{-4}$ , which is gradually reduced to  $1 \times 10^{-6}$  via the cosine annealing strategy [24].

**Datasets:** (1) *LSRW-Huawei* is a subset of the LSRW [15] dataset consisting of images captured by Huawei smartphones, which includes 2450 pairs of training images and

Table 1. Experiment results on the LSRW-Huawei, LOLv2, and SDSD test benchmarks. The background color gradients from dark to light, with red indicating the optimal result, orange denoting the sub-optimal result, and yellow following in order.

Method	Params	GFLOPs	LSRW-Huawei			LOLv2.Real			LOLv2.Syn			SDSD_indoor			SDSD_outdoor		
			PSNR↑	SSIM↑	NIQE↓	PSNR↑	SSIM↑	NIQE↓	PSNR↑	SSIM↑	NIQE↓	PSNR↑	SSIM↑	NIQE↓	PSNR↑	SSIM↑	NIQE↓
RetinexNet [46]	0.8	587.47	15.61	0.414	7.235	16.10	0.407	9.425	17.14	0.756	5.405	20.84	0.617	7.924	20.96	0.629	9.947
KinD [53]	8.0	34.99	15.77	0.548	5.517	18.67	0.772	9.221	15.22	0.542	6.124	20.98	0.597	7.221	21.65	0.621	8.714
RRDNet [55]	0.1	2.10	14.66	0.541	7.725	15.21	0.514	9.912	16.67	0.667	4.894	21.07	0.601	6.921	20.04	0.647	8.997
Zero-DCE [12]	0.7	5.21	14.86	0.559	4.215	14.12	0.512	8.652	14.93	0.531	5.507	21.23	0.752	6.941	20.39	0.691	8.014
SCI [27]	0.09	0.06	14.78	0.526	3.667	17.30	0.541	8.077	14.96	0.721	4.899	20.43	0.714	6.574	21.33	0.701	7.778
LLFormer [42]	13.2	22.52	16.23	0.642	3.947	20.56	0.801	9.162	24.42	0.914	4.614	25.66	0.832	6.627	28.45	0.821	8.011
UHDFormer [39]	0.3	48.37	21.07	0.604	4.621	21.59	0.804	7.230	22.60	0.903	5.476	28.13	0.875	7.021	22.75	0.732	6.657
Retinexformer [4]	1.6	15.51	22.24	0.701	2.976	21.65	0.835	4.735	25.10	0.925	3.971	28.96	0.879	5.441	28.96	0.896	7.201
IAT [8]	0.09	1.44	20.12	0.694	4.217	20.30	0.752	5.232	22.96	0.856	5.512	19.97	0.713	4.177	19.97	0.711	6.417
WalMaFa [37]	39.7	14.41	21.04	0.698	3.112	22.49	0.851	4.365	25.10	0.945	4.275	29.67	0.915	3.541	28.94	0.891	3.955
MambaR [13]	20.4	60.66	21.14	0.704	3.004	20.11	0.802	4.928	24.75	0.922	4.522	25.11	0.873	3.661	26.35	0.510	4.477
RetinexMamba [2]	4.6	34.75	20.88	0.629	3.104	22.34	0.826	4.771	24.71	0.932	4.503	28.21	0.893	3.976	26.22	0.866	4.011
MambaLLIE [47]	4.4	20.85	20.64	0.627	3.047	22.14	0.821	4.021	24.81	0.940	4.071	29.74	0.902	4.417	28.92	0.869	4.417
<b>DRWKV (Ours)</b>	9.7	1.67	22.34	0.703	2.944	24.12	0.832	3.926	25.02	0.947	3.941	30.26	0.922	3.441	28.96	0.891	3.954

30 pairs of test images. (2) *LOLv2* [50] is divided into two subsets: *LOLv2 Real* and *LOLv2 Synthetic*. The former is a dataset of real low-light scenes, containing 689 pairs of training images and 100 pairs of test images, covering various environments such as campuses and clubs. The latter is a synthetic dataset, consisting of 900 pairs of training images and 100 pairs of test images. (3) *SDSD* [41] dataset has two subsets: indoor and outdoor. The indoor subset includes 62 pairs of low-light/normal-light videos for training and 6 pairs of low-light/normal-light videos for testing. The outdoor subset contains 116 pairs of low-light/normal-light videos for training and 10 pairs of low-light/normal-light videos for testing.

**Metrics:** We use traditional quality (distortion) metrics PSNR and SSIM [44] to evaluate the results of LLIE, aiming to measure the pixel-level similarity and distortion between the enhanced images and reference images. Additionally, NIQE [29] is employed to assess the no-reference perceptual quality of the enhanced images.

## 4.2. Comparative Experiments

**Model Comparison Results:** Based on the quantitative results across five test benchmarks, the DRWKV model achieves performance improvements over multiple baseline methods with extremely low GFLOPs, as shown in Table 1. Specifically, DRWKV exhibits superior performance in terms of naturalness on *LSRW-Huawei*, characterized by low baseline values of NIQE and a high optimization rate (achieves a 1.1% optimization compared to the second-place method). Additionally, on *LOLv2*, DR-

WKV shows differences in optimization strengths between the Real and Synthetic test benchmarks: it achieves the optimal model performance with an average improvement of 5.00 dB in PSNR on Real and 0.152 in SSIM on Synthetic, balancing the enhancement of image quality and the preservation of structural information. In low-light scenario videos, by independently enhancing low-light frames in *SDSD*, the model demonstrates average PSNR differences of up to 9.42 dB/8 dB in indoor and outdoor scenes, ensuring high “restoration accuracy” of image details. For visualization results, refer to Figure 3; the generated results of our DRWKV model exhibit continuous object edges and high-fidelity details, which are highly consistent with the subject-focused edges.

Table 2. Comparison of different Block combinations on the *LOLv2 Real* benchmark dataset.

Config	Block1	Block2	PSNR↑	SSIM↑	NIQE↓
(I)	Robust Retinex	Robust Retinex	22.57	0.741	4.124
<b>Ours</b>	Robust Retinex	GER	24.12	0.832	3.926

**Retinex Configuration Results:** This experiment focuses on the contradiction of edge distortion under low light. In terms of network structure, replaceable structures Block1 and Block2 are preset to assist in configuring Retinex, enabling DRWKV to achieve global optimum. Since the input end of the GER theory needs to receive the edge feature  $E$  (a parameter from the output end of DRWKV), Block1 is constrained by structural limitations. To minimize distur-

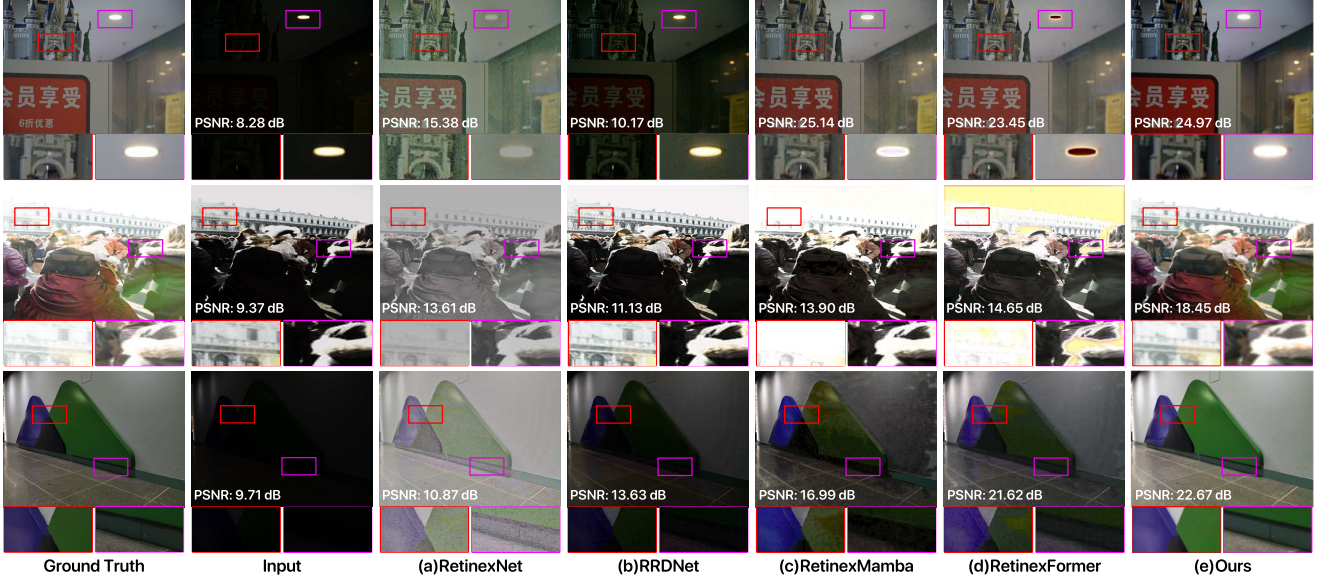


Figure 3. Visualization results of RetinexNet, RRDNet, RetinexMamba, RetinexFormer, and DRWKV on the LOLv2-Real, LOLv2-Synthetic, and LSRW-Huawei datasets respectively (zoom in to display details for each model).

bance to the network architecture, one-sided fixation is ultimately adopted. Deploying the GER theory into Block2 results in remarkable improvement rates of 6.9%/12.3%/4.8% for PSNR, SSIM, and NIQE, respectively, as shown in Table 2. This strongly validates the core idea of gradient-guided global-edge coupling in the GER theory, demonstrating its strong practicality in addressing edge issues of low-light images and further confirming *Hypothesis(1)*.

### 4.3. Ablation Studies

**Loss Performance Results:** A targeted ablation study was performed on the proposed loss function combinations. In Figure 4(a), the absence of the decompositional consistency loss  $\mathcal{L}_{recon}$  results in an overall darker reconstructed image with incomplete edge information, indirectly validating its role in structural and luminance reconstruction. In Figure 4(b), removing the edge sparsity loss  $\mathcal{L}_{sparse}$  leads to false edges generated by Gaussian noise contaminating flat regions, highlighting its contribution to preserving and enhancing low-light edges. Figures 4(c) and 4(d) illustrate uneven illumination and over-denoising effects caused by the removal of the illumination smoothness loss  $\mathcal{L}_{smooth}$  and artifact suppression loss  $\mathcal{L}_{artifact}$ , respectively, confirming their balancing roles. Figure 4(e) demonstrates model instability with negative image artifacts when the parameter regularization loss  $\mathcal{L}_{reg}$  is removed, indicating that effective regularization can improve the model’s adaptability to unseen data. Additionally, the loss parameters for this model are specified as follows:  $\lambda_1 = 1$ ,  $\lambda_2 = 0.01$ ,  $\lambda_3 = 0.1$ ,  $\lambda_4 = 0.05$ , and  $\lambda_5 = 1e - 4$ .

**Component Ablation Results:** This experiment aims to verify the effectiveness of the Evolving Scanning mechanism proposed in *Hypothesis(2)* for the edges of low-light images. Structurally, a progressive component integration strategy is adopted, with LOLv2 Real as the test benchmark and the basic structure as the test framework, to construct a five-level progressive validation system. The component configurations, ablation variables, and validation results at each level are shown in Table 3. In terms of the basic structure, we retain the ViT-style block stacking structure of VRWKV and introduce the SSIM+L1 loss, enabling it to initially possess the capability to handle low-light issues. However, the model exhibits nearly ineffective feature extraction in illumination-degraded scenarios, characterized by extremely low SSIM (0.415) and PSNR (12.57 dB) values.

Validation (1): After embedding the Evolving Scanning module (ES-RWKV), the performance of SSIM and PSNR increased by 42.4% and 29.4%, respectively. This explicitly verifies that the proposed spiral scanning is compatible with the edge spatial topology, capable of ensuring the continuity of edges of low-light objects.

Validation (2): By modifying the network from the ViT-style block stacking scheme to a UNet-like scheme, the model performance optimization focuses on detail accuracy. At the cost of a certain increase in parameter count and computational load, the PSNR index gains 3.16 dB.

Validation (3): Adding a light preprocessing(LP) stage leads to a slight increase in image quality evaluation metrics, demonstrating that this stage contributes to improving



Figure 4. An ablation study is conducted on the proposed decompositional consistency loss  $L_{recon}$ , edge sparsity loss  $L_{sparse}$ , illumination smoothness loss  $L_{smooth}$ , artifact suppression loss  $L_{artifact}$ , and parameter regularization loss  $L_{reg}$ .

pixel errors and structures.

Validation (4): Embedding the Bi-SAB module and adopting high-performance multi-module cascading significantly optimize the model structure. The parameter count and computational load are drastically reduced by 49.3% and 43.8%, respectively, while SSIM and PSNR achieve beneficial gains of 0.028 and 0.8 dB, endowing the model with basic lightweight characteristics.

Validation (5): Replacing the SSIM+L1 loss with the proposed  $MS^2$ -Loss specifically optimizes the training process, with SSIM and PSNR optimized to 0.832 and 24.12 dB, respectively.

At this point, the hypotheses proposed in the Methodology have been fully validated. The paper constructs a complete research closed-loop from four dimensions: theory, technology, experiment, and application.

Table 3. Ablation study on the LOLv2 Real benchmark dataset. If the RWKV blocks and training losses are not selected, Bi-RWKV and SSIM+L1 loss will be used by default. ✗ denotes the use of a ViT-style block stacking structure, whereas ✓ indicates the adoption of a UNet-like architecture.

ES-RWKV	LP	Bi-SAB	$MS^2$ -Loss	SSIM↑	PSNR↑	Params.(M)	GFLOPs
				0.415	12.57	10.51	0.02
✗				0.591	16.27	14.57	2.65
✓				0.607	19.43	16.36	2.95
✓	✓			0.748	22.67	16.36	2.97
✓	✓	✓		0.776	23.47	8.29	1.67
✓	✓	✓	✓	0.832	24.12	8.28	1.67

#### 4.4. Extended Validation

To evaluate generalization, we applied DRWKV to low-light multi-object tracking on the UAVDark135 benchmark [18], comprising 135 sequences across diverse scenarios at 30 FPS and 1920×1080 resolution.

Mainstream tracking algorithms were tested with and without DRWKV, using MOTA, IDF1, and HOTA as metrics. DRWKV consistently improved performance, notably in identity preservation. ByteTrack saw gains of

5.189%/3.076%/2.705%, while BoT-SORT and others improved by 1.5%–7%.

In contrast, Deep OC-SORT showed mixed results, with improved MOTA but reduced IDF1, suggesting structural sensitivity to enhanced features. Implementation details are provided in the Appendix.

Table 4. Extended validation results of DRWKV on low-light object tracking performance. MOTA [3], IDF1 [34] and HOTA [26] are common performance evaluation metrics for object tracking.

Methods	w/o LLIE Module			DRWKV (Ours)		
	MOTA(%)	IDF1(%)	HOTA(%)	MOTA(%)	IDF1(%)	HOTA(%)
ByteTrack [52]	23.434	62.776	50.117	28.623	65.852	52.822
BoT-SORT [1]	18.242	62.916	49.556	25.496	64.049	51.435
Hybrid-SORT [49]	20.684	62.054	49.196	29.355	66.365	52.905
OC-SORT [5]	21.062	62.967	49.469	28.102	66.000	52.501
Deep OC-SORT [28]	19.514	63.205	49.857	24.929	58.016	49.124
StrongSORT [9]	20.923	53.583	45.553	25.148	64.677	51.842

## 5. Conclusion

In this study, we introduced the DRWKV model to address the challenge of preserving edge details in Low-Light Image Enhancement (LLIE). By integrating the Global Edge Retinex (GER) theory, the model decouples illumination and edge structures, ensuring high-fidelity edge continuity even in extreme low-light conditions. The Evolving WKV Attention mechanism enhances spatial edge continuity, while the Bilateral Spectrum Aligner Block (Bi-SAB) and  $MS^2$ -Loss optimize luminance and chrominance alignment, reducing artifacts and improving visual quality. Extensive experiments on benchmark datasets show that DRWKV outperforms existing methods in PSNR, SSIM, and NIQE, with lower computational cost. Additionally, it proves effective in tasks like low-light multi-object tracking, enhancing performance, especially in identity preservation. Future work will focus on adapting DRWKV for mobile platforms and further improving its robustness across various low-light scenarios, bridging the gap between academic research and real-world deployment.

## References

- [1] Nir Aharon, Roy Orfaig, and Ben-Zion Bobrovsky. Bot-sort: Robust associations multi-pedestrian tracking. *arXiv preprint arXiv:2206.14651*, 2022. [8](#)
- [2] Jiesong Bai, Yuhao Yin, Qiyuan He, Yuanxian Li, and Xiaofeng Zhang. Retinexmamba: Retinex-based mamba for low-light image enhancement. In *International Conference on Neural Information Processing*, pages 427–442. Springer, 2024. [1](#), [2](#), [6](#)
- [3] Keni Bernardin and Rainer Stiefelhagen. Evaluating multiple object tracking performance: the clear mot metrics. *EURASIP Journal on Image and Video Processing*, 2008(1):246309, 2008. [8](#)
- [4] Yuanhao Cai, Hao Bian, Jing Lin, Haoqian Wang, Radu Timofte, and Yulun Zhang. Retinexformer: One-stage retinex-based transformer for low-light image enhancement. In *Proceedings of the IEEE/CVF international conference on computer vision*, pages 12504–12513, 2023. [2](#), [6](#)
- [5] Jinkun Cao, Jiangmiao Pang, Xinshuo Weng, Rawal Khirrodkar, and Kris Kitani. Observation-centric sort: Rethinking sort for robust multi-object tracking. In *Proceedings of the IEEE/CVF Conference on Computer Vision and Pattern Recognition (CVPR)*, pages 9686–9696, June 2023. [8](#)
- [6] Mengting Chen, Shi Yi, Lang Wu, Hongli Yin, and Ling Chen. Highly robust thermal infrared and visible image registration with canny and phase congruence detection. *Optics and Lasers in Engineering*, 183:108526, 2024. [2](#)
- [7] Xianmin Chen, Peiliang Huang, Xiaoxu Feng, Dingwen Zhang, Longfei Han, and Junwei Han. Retinex-rawmamba: Bridging demosaicing and denoising for low-light raw image enhancement. *arXiv preprint arXiv:2409.07040*, 2024. [2](#)
- [8] Ziteng Cui, Kunchang Li, Lin Gu, Shenghan Su, Peng Gao, Zhengkai Jiang, Yu Qiao, and Tatsuya Harada. You only need 90k parameters to adapt light: a light weight transformer for image enhancement and exposure correction. *arXiv preprint arXiv:2205.14871*, 2022. [6](#)
- [9] Yunhao Du, Zhicheng Zhao, Yang Song, Yanyun Zhao, Fei Su, Tao Gong, and Hongying Meng. Strongsort: Make deepsort great again. *IEEE Transactions on Multimedia*, 25:8725–8737, 2023. [8](#)
- [10] Yuchen Duan, Weiyun Wang, Zhe Chen, Xizhou Zhu, Lewei Lu, Tong Lu, Yu Qiao, Hongsheng Li, Jifeng Dai, and Wenhai Wang. Vision-rwkv: Efficient and scalable visual perception with rwkv-like architectures. *arXiv preprint arXiv:2403.02308*, 2024. [1](#)
- [11] Yurong GUAN, Muhammad Aamir, Ziaur Rahman, Zaheer Ahmed Dayo, Waheed Ahmed Abro, Muhammad Ishfaq, and Zhihua HU. A dual-tree complex wavelet transform-based model for low-illumination image enhancement. *Wuhan University Journal of Natural Sciences*, 26(05):405–414, 2021. [2](#)
- [12] Chunle Guo, Chongyi Li, Jichang Guo, Chen Change Loy, Junhui Hou, Sam Kwong, and Runmin Cong. Zero-reference deep curve estimation for low-light image enhancement. In *Proceedings of the IEEE/CVF conference on computer vision and pattern recognition*, pages 1780–1789, 2020. [1](#), [2](#), [6](#)
- [13] Hang Guo, Jinmin Li, Tao Dai, Zhihao Ouyang, Xudong Ren, and Shu-Tao Xia. Mambair: A simple baseline for image restoration with state-space model. In *European conference on computer vision*, pages 222–241. Springer, 2024. [6](#)
- [14] Xiaojie Guo, Yu Li, and Haibin Ling. Lime: Low-light image enhancement via illumination map estimation. *IEEE Transactions on image processing*, 26(2):982–993, 2016. [1](#)
- [15] Jiang Hai, Zhu Xuan, Ren Yang, Yutong Hao, Fengzhu Zou, Fang Lin, and Songchen Han. R2rnet: Low-light image enhancement via real-low to real-normal network. *Journal of Visual Communication and Image Representation*, 90:103712, 2023. [5](#)
- [16] G. E. Hinton and R. R. Salakhutdinov. Reducing the dimensionality of data with neural networks. *Science*, 313(5786):504–507, 2006. [5](#)
- [17] Diederik P Kingma and Jimmy Ba. Adam: A method for stochastic optimization. *arXiv preprint arXiv:1412.6980*, 2014. [5](#)
- [18] Bowen Li, Changhong Fu, Fangqiang Ding, Junjie Ye, and Fuling Lin. All-day object tracking for unmanned aerial vehicle, 2021. [8](#)
- [19] Dong Li, Jiaying Zhu, Menglu Wang, Jiawei Liu, Xueyang Fu, and Zheng-Jun Zha. Edge-aware regional message passing controller for image forgery localization. In *Proceedings of the IEEE/CVF Conference on Computer Vision and Pattern Recognition*, pages 8222–8232, 2023. [2](#)
- [20] Mading Li, Jiaying Liu, Wenhan Yang, Xiaoyan Sun, and Zongming Guo. Structure-revealing low-light image enhancement via robust retinex model. *IEEE Transactions on Image Processing*, 27(6):2828–2841, 2018. [1](#)
- [21] Seokjae Lim and Wonjun Kim. Dslr: Deep stacked laplacian restorer for low-light image enhancement. *IEEE Transactions on Multimedia*, 23:4272–4284, 2020. [2](#)
- [22] Zibin Liu, Banglei Guan, Yang Shang, Shunkun Liang, Zhenbao Yu, and Qifeng Yu. Optical flow-guided 6dof object pose tracking with an event camera. In *Proceedings of the 32nd ACM International Conference on Multimedia*, pages 6501–6509, 2024. [2](#)
- [23] Kin Gwn Lore, Adedotun Akintayo, and Soumik Sarkar. Llnet: A deep autoencoder approach to natural low-light image enhancement. *Pattern Recognition*, 61:650–662, 2017. [2](#)
- [24] Ilya Loshchilov and Frank Hutter. Sgdr: Stochastic gradient descent with warm restarts. *arXiv preprint arXiv:1608.03983*, 2016. [5](#)
- [25] Yuxu Lu, Yuan Gao, Yongqi Guo, Wenyu Xu, and Xianjun Hu. Low-light image enhancement via gradient prior-aided network. *IEEE Access*, 10:92583–92596, 2022. [2](#)
- [26] Jonathon Luiten, Aljosa Osep, Patrick Dendorfer, Philip Torr, Andreas Geiger, Laura Leal-Taixé, and Bastian Leibe. Hota: A higher order metric for evaluating multi-object tracking. *International journal of computer vision*, 129(2):548–578, 2021. [8](#)
- [27] Long Ma, Tengyu Ma, Risheng Liu, Xin Fan, and Zhongxuan Luo. Toward fast, flexible, and robust low-light image enhancement. In *Proceedings of the IEEE/CVF conference on computer vision and pattern recognition*, pages 5637–5646, 2022. [6](#)

- [28] Gerard Maggolino, Adnan Ahmad, Jinkun Cao, and Kris Kitani. Deep oc-sort: Multi-pedestrian tracking by adaptive re-identification. In *2023 IEEE International conference on image processing (ICIP)*, pages 3025–3029. IEEE, 2023. 8
- [29] Anish Mittal, Rajiv Soundararajan, and Alan C. Bovik. Making a “completely blind” image quality analyzer. *IEEE Signal Processing Letters*, 20(3):209–212, 2013. 6
- [30] Cindy M Nguyen, Eric R Chan, Alexander W Bergman, and Gordon Wetzstein. Diffusion in the dark: A diffusion model for low-light text recognition. In *Proceedings of the IEEE/CVF Winter Conference on Applications of Computer Vision*, pages 4146–4157, 2024. 1
- [31] Mengyang Pu, Yaping Huang, Yuming Liu, Qingji Guan, and Haibin Ling. Edter: Edge detection with transformer. In *Proceedings of the IEEE/CVF conference on computer vision and pattern recognition*, pages 1402–1412, 2022. 2
- [32] HE Qian and LIU Boyun. Improved infrared image edge detection algorithm based on dexined. *Infrared Technology*, 43(9):876–884, 2021. 2
- [33] Jingxiang Qu, Ryan Wen Liu, Yuan Gao, Yu Guo, Fenghua Zhu, and Fei-Yue Wang. Double domain guided real-time low-light image enhancement for ultra-high-definition transportation surveillance. *IEEE Transactions on Intelligent Transportation Systems*, 25(8):9550–9562, 2024. 1
- [34] Ergys Ristani, Francesco Solera, Roger Zou, Rita Cucchiara, and Carlo Tomasi. Performance measures and a data set for multi-target, multi-camera tracking. In *European conference on computer vision*, pages 17–35. Springer, 2016. 8
- [35] Xiaoke Shang, Gehui Li, Zhiying Jiang, Shaomin Zhang, Nai Ding, and Jinyuan Liu. Holistic dynamic frequency transformer for image fusion and exposure correction. *Information Fusion*, 102:102073, 2024. 1
- [36] Yiqi Shi, Duo Liu, Liguang Zhang, Ye Tian, Xuezhi Xia, and Xiaojing Fu. Zero-ig: zero-shot illumination-guided joint denoising and adaptive enhancement for low-light images. In *Proceedings of the IEEE/CVF conference on computer vision and pattern recognition*, pages 3015–3024, 2024. 1
- [37] Junhao Tan, Songwen Pei, Wei Qin, Bo Fu, Ximing Li, and Libo Huang. Wavelet-based mamba with fourier adjustment for low-light image enhancement. In *Proceedings of the Asian Conference on Computer Vision (ACCV)*, pages 3449–3464, December 2024. 1, 6
- [38] Xu Tang, Yuexi Yao, Jingjing Ma, Xiangrong Zhang, Yuqun Yang, Bo Wang, and Licheng Jiao. Spiralmamba: Spatial-spectral complementary mamba with spatial spiral scan for hyperspectral image classification. *IEEE Transactions on Geoscience and Remote Sensing*, 2025. 2
- [39] Cong Wang, Jinshan Pan, Wei Wang, Gang Fu, Siyuan Liang, Mengzhu Wang, Xiao-Ming Wu, and Jun Liu. Correlation matching transformation transformers for uhd image restoration. In *Proceedings of the AAAI Conference on Artificial Intelligence*, volume 38, pages 5336–5344, 2024. 6
- [40] Kun Wang, Xiaohong Zhang, Xiangbo Zhang, Yuting Lu, Sheng Huang, and Dan Yang. Eanet: Iterative edge attention network for medical image segmentation. *Pattern Recognition*, 127:108636, 2022. 2
- [41] Ruixing Wang, Xiaogang Xu, Chi-Wing Fu, Jiangbo Lu, Bei Yu, and Jiaya Jia. Seeing dynamic scene in the dark: A high-quality video dataset with mechatronic alignment. In *2021 IEEE/CVF International Conference on Computer Vision (ICCV)*, pages 9680–9689, 2021. 6
- [42] Tao Wang, Kaihao Zhang, Tianrun Shen, Wenhan Luo, Bjorn Stenger, and Tong Lu. Ultra-high-definition low-light image enhancement: A benchmark and transformer-based method. In *Proceedings of the AAAI conference on artificial intelligence*, volume 37, pages 2654–2662, 2023. 6
- [43] Yu Wang, Fei Wang, Kun Li, Xuping Feng, Wenhui Hou, Lu Liu, Liqing Chen, Yong He, and Yuwei Wang. Low-light wheat image enhancement using an explicit inter-channel sparse transformer. *Computers and Electronics in Agriculture*, 224:109169, 2024. 1
- [44] Zhou Wang, A.C. Bovik, H.R. Sheikh, and E.P. Simoncelli. Image quality assessment: from error visibility to structural similarity. *IEEE Transactions on Image Processing*, 13(4):600–612, 2004. 6
- [45] Zhen Wang, Dongyuan Li, Guang Li, Ziqing Zhang, and Renhe Jiang. Multimodal low-light image enhancement with depth information. In *Proceedings of the 32nd ACM International Conference on Multimedia*, pages 4976–4985, 2024. 1
- [46] Chen Wei, Wenjing Wang, Wenhan Yang, and Jiaying Liu. Deep retinex decomposition for low-light enhancement. *arXiv preprint arXiv:1808.04560*, 2018. 2, 6
- [47] Jiangwei Weng, Zhiqiang Yan, Ying Tai, Jianjun Qian, Jian Yang, and Jun Li. Mamballie: Implicit retinex-aware low light enhancement with global-then-local state space. *Advances in Neural Information Processing Systems*, 37:27440–27462, 2024. 6
- [48] Lintao Xu, Changhui Hu, Yin Hu, Xiaoyuan Jing, Ziyun Cai, and Xiaobo Lu. Upt-flow: Multi-scale transformer-guided normalizing flow for low-light image enhancement. *Pattern Recognition*, 158:111076, 2025. 1
- [49] Mingzhan Yang, Guangxin Han, Bin Yan, Wenhua Zhang, Jinqing Qi, Huchuan Lu, and Dong Wang. Hybrid-sort: Weak cues matter for online multi-object tracking. In *Proceedings of the AAAI conference on artificial intelligence*, volume 38, pages 6504–6512, 2024. 8
- [50] Wenhan Yang, Wenjing Wang, Haofeng Huang, Shiqi Wang, and Jiaying Liu. Sparse gradient regularized deep retinex network for robust low-light image enhancement. *IEEE Transactions on Image Processing*, 30:2072–2086, 2021. 2, 6
- [51] Jin Zhang, Haiyan Jin, Haonan Su, Yuanlin Zhang, Zhaolin Xiao, and Bin Wang. A cnn-transformer network based snr guided high frequency reconstruction for low light image enhancement. In *2024 IEEE International Conference on Image Processing (ICIP)*, pages 1649–1655. IEEE, 2024. 1
- [52] Yifu Zhang, Peize Sun, Yi Jiang, Dongdong Yu, Fucheng Weng, Zehuan Yuan, Ping Luo, Wenyu Liu, and Xinggang Wang. Bytetrack: Multi-object tracking by associating every detection box. In *European conference on computer vision*, pages 1–21. Springer, 2022. 8
- [53] Yonghua Zhang, Jiawan Zhang, and Xiaojie Guo. Kindling the darkness: A practical low-light image enhancer. In *Proceedings of the 27th ACM international conference on multimedia*, pages 1632–1640, 2019. 6

- [54] Mengjie Zhao and Olga Fink. Dyedgegat: Dynamic edge via graph attention for early fault detection in iiot systems. *IEEE Internet of Things Journal*, 2024. [2](#)
- [55] Anqi Zhu, Lin Zhang, Ying Shen, Yong Ma, Shengjie Zhao, and Yicong Zhou. Zero-shot restoration of underexposed images via robust retinex decomposition. In *2020 IEEE International Conference on Multimedia and Expo (ICME)*, pages 1–6, 2020. [6](#)
- [56] Wenbin Zou, Hongxia Gao, Weipeng Yang, and Tongtong Liu. Wave-mamba: Wavelet state space model for ultra-high-definition low-light image enhancement. In *Proceedings of the 32nd ACM International Conference on Multimedia*, pages 1534–1543, 2024. [1](#)

# DRWKV: Focusing on Object Edges for Low-Light Image Enhancement

## Appendices & Supplementary Material

### 6. Supplementary Experiments

In this appendix, we first present a comprehensive exposition of the core computational pipeline of the DRWKV model introduced in the main text, together with the detailed implementation specifics of each key module. Subsequently, to rigorously validate the enhanced capabilities claimed by the proposed DRWKV model, we designed a series of extended experiments; the experimental protocol and the corresponding analyses of the results are elaborated in the ensuing sections.

### 7. Architecture Details of DRWKV

In this section, we provide a detailed exposition of the Light Preprocessing pipeline introduced in Section 3, the ES-RWKV computational flow, and the constituent fine-grained modules.

#### 7.1. Light Preprocessing

Light Preprocessing takes a low-light image  $I \in \mathbb{R}^{3 \times H \times W}$  as input. First, under the gray-world hypothesis, it computes the global illumination component  $L_{\text{ill}} \in \mathbb{R}^{C \times H \times W}$ . This hypothesis assumes that, in a color-balanced scene, the average reflectance of all pixels tends toward neutral gray. Guided by this assumption, the global illumination map  $L_{\text{ill}}$ , which characterizes the spatial distribution of overall illumination intensity, is derived from the input image  $I$  and serves as the basis for the final enhancement.

The input image  $I$  is initially processed by a depthwise-separable  $3 \times 3$  convolution layer with ReLU activation. The resulting feature map is then fed in parallel into three independent  $1 \times 1$  convolution modules, each with a distinct activation function to produce specific components: a module with Sigmoid activation outputs the structured artifact component  $S \in \mathbb{R}^{3 \times H \times W}$ , intended to capture potential structured interference patterns; a module with Sigmoid activation outputs the noise estimation component  $N \in \mathbb{R}^{3 \times H \times W}$ , quantifying the noise contamination level; and a module with Tanh activation outputs the local illumination estimation component  $L \in \mathbb{R}^{1 \times H \times W}$ , providing a finer, spatially adaptive representation of illumination intensity. The procedure is as follows:

$$B(I) = \text{ReLU}(\text{DepthConv}_{3 \times 3}(I)), \quad (17)$$

$$S = \text{Sigmoid}(\text{Conv}_{1 \times 1}(B^3(I))), \quad (18)$$

$$L = \text{Sigmoid}(\text{Conv}_{1 \times 1}(B^3(I))), \quad (19)$$

$$N = \text{Tanh}(\text{Conv}_{1 \times 1}(B^3(I))), \quad (20)$$

where  $\text{DepthConv}_{3 \times 3}(\cdot)$  denotes the  $3 \times 3$  depthwise convolution,  $\text{Conv}_{1 \times 1}(\cdot)$  denotes the  $1 \times 1$  convolution,  $\text{ReLU}(\cdot)$ ,  $\text{Sigmoid}(\cdot)$ , and  $\text{Tanh}(\cdot)$  are the respective activation functions, and  $B^3(\cdot)$  denotes three consecutive applications of  $B(\cdot)$ .

The noise estimation  $N$ , illumination estimation  $L$ , and the original input  $I$  are combined via

$$\hat{R} = \frac{I - N}{L}, \quad (21)$$

yielding the reconstructed reflectance  $\hat{R} \in \mathbb{R}^{3 \times H \times W}$ . Then,  $I$  and  $\hat{R}$  are combined to obtain the enhanced image  $\hat{I} \in \mathbb{R}^{3 \times H \times W}$ :

$$\hat{I} = I \odot \hat{R}, \quad (22)$$

where  $\odot$  denotes element-wise multiplication.

#### 7.2. Evolving Scanning RWKV

Unlike traditional spatial modelling approaches, the proposed ES-RWKV breaks through spatial-size constraints, preserves structural integrity, enhances modelling capacity, and enables cross-space information interaction while markedly reducing the computational overhead of handling complex spatial features, thereby offering an efficient solution for spatial feature extraction and fusion in vision tasks. The ES-RWKV block is decomposed into two sequential stages: Evolving Scanning Spatial Mix and Channel Mix. The Evolving Scanning RWKV structure is shown in Figure.5

##### 7.2.1 Evolving Scanning Spatial Mix

They tackles the dilemma between spatial-size limits and structural integrity. A channel-wise Q-Shift allows the model to adapt flexibly to different tasks without extra computation. Coupled with the EV-WKV mechanism, an embedded eight-spiral scanning pattern is introduced to

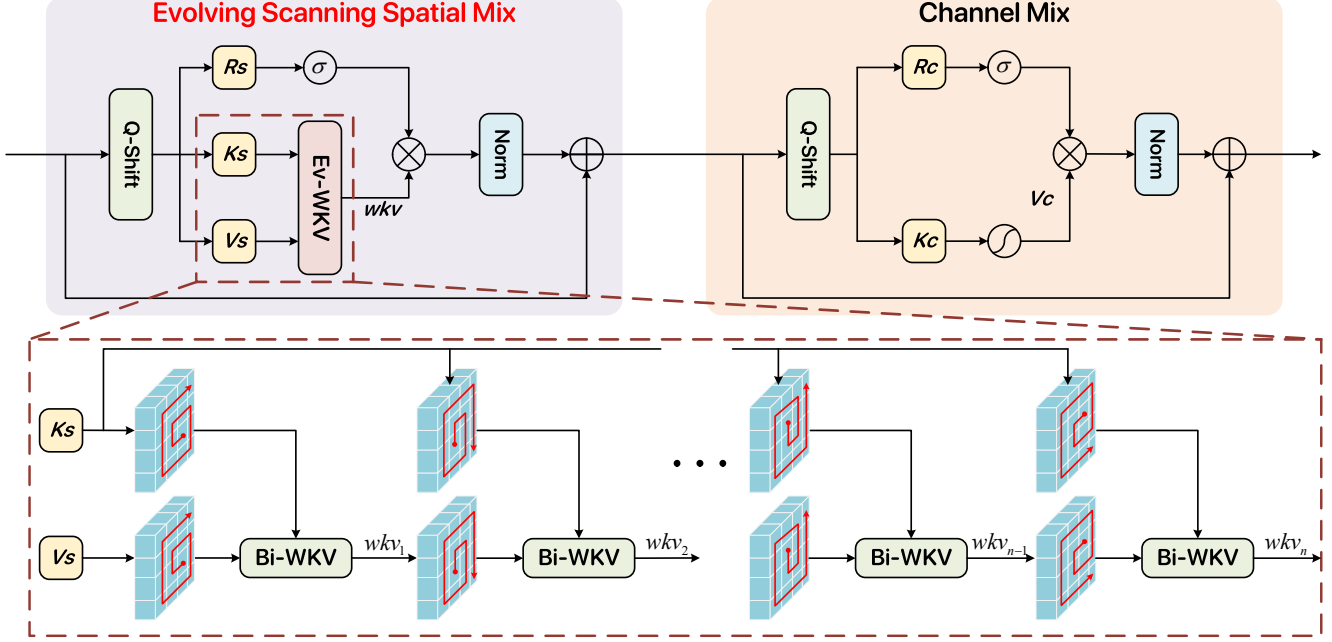


Figure 5. Evolving Scanning RWKV's structure, it consists of two parts: Evolving Scanning Spatial Mix and Channel Mix.

capture spatial dependencies more comprehensively and efficiently, suppressing redundancy irrelevant to spatial extraction. Spatial information is then consolidated by a LayerNorm, enabling the model to automatically emphasize salient features and attenuate noise, thereby facilitating downstream layers in learning effective spatial patterns.

For an input feature  $X \in \mathbb{R}^{T \times C}$ , we augment the standard sequential processing framework with a channel-partitioned Q-Shift mechanism. By slicing and concatenating along the channel axis, we construct a shifted feature  $X^\dagger$ . Incorporating the learnable vector  $\mu_{(*)}$ , we dynamically interpolate and fuse the original feature  $X$  and the shifted feature  $X^\dagger$  to further transcend the spatial size limitations of traditional methods, preserve the integrity of spatial structures, and enhance the model's capability to capture cross-spatial positional information. This process yields feature components tailored for spatial mixing computations:

$$Q\text{-Shift}_{(*)}(X) = X + (1 - \mu_{(*)})X^\dagger \quad (23)$$

$$X^\dagger[h, w] = \text{Concat}(X[h-1, w, 0 : C/4], \\ X[h+1, w, C/4 : C/2], \\ X[h, w-1, C/2 : 3C/4], \\ X[h, w+1, 3C/4 : C]) \quad (24)$$

In this context,  $(*) \in \{R, K, V\}$  denotes three types of interpolation operations performed on  $X$  and  $X^\dagger$ . These operations are governed by  $\mu$  and are utilized for the subsequent computation of  $R$ ,  $K$ , and  $V$ . Here,  $h$ ,  $w$ , and  $C$  represent the height, width, and number of channels, respectively.

represent the height, width, and number of channels, respectively.

Subsequently, after the Q-Shift operation  $X$  is decomposed into three independent components  $R_s, K_s, V_s \in \mathbb{R}^{T \times C}$

$$(*)_s = Q\text{-Shift}_{(*)}(X)W_{(*)} = (X + (1 - \mu_{(*)})X^\dagger)W_{(*)} \quad (25)$$

$W_{(*)}$  denotes the weight. To ensure numerical stability, prevent training divergence, and accelerate training convergence, we introduce the LN layer. The total output of the Evolving Scanning Spatial Mix block is as follows:

$$O_s = X + \text{LN}((\sigma(R_s) \odot wkv)W_{O_s}), \quad (26)$$

$$\text{where } wkv = \text{EV-WKV}(K_s, V_s), \quad (27)$$

Here,  $\sigma$  denotes the sigmoid activation function,  $\odot$  represents the element-wise multiplication operation, LN denotes layer normalization, and  $W_{O_s}$  denotes the weight. EV-WKV is an Evolving Scanning Mechanism proposed based on the linear scanning formula  $wkvt$  of Bi-WKV.

## 7.2.2 Channel Mix

We reintroduce the Q-Shift mechanism and combine it with the SquaredReLU activation function and linear projection. This is aimed at addressing the shortcomings that may exist after the spatial mixing in the first stage, such as insufficient exploration of correlations between channel features and oversimplified feature expression. It ensures

more adequate feature fusion in the channel dimension, enhances the nonlinear expression ability and discriminability of features, and further maintains the stability of numerical distribution through Layer Normalization (LN), thereby providing richer and more robust inputs for feature learning in the deep layers of the model.

First, we take the feature  $O_s$  output from the first stage as input, and construct the query feature  $R_c$  and key feature  $K_c$  for channel interaction respectively through the Q-Shift mechanism. The calculation process is as follows:

$$\begin{aligned} R_c &= Q - Shift_R(O_s)W_R, \\ K_c &= Q - Shift_K(O_s)W_K \end{aligned} \quad (28)$$

Here,  $Q-Shift_R$  and  $Q-Shift_K$  dynamically interpolate between the original feature  $O_s$  and its shifted version  $O_s^\dagger$  using learnable parameters  $\mu_{(R)}$  and  $\mu_{(K)}$ . This design not only preserves the spatial structural information in the original features but also introduces cross-position channel dependencies, enabling the model to adaptively focus on long-range correlations among different channels.

Subsequently, to enhance the nonlinear expression capability of features and alleviate the gradient vanishing problem, the *SquaredReLU* activation function is applied to for  $K_c$  transformation.

Further, the transformed features are projected into the value space via linear projection, and the output of the Channel Mix module is generated through residual connections and layer normalization operations. The detailed process is as follows:

$$O_c = O_s + LN((\sigma(R_c) \odot V_c)W_{O_c}), \quad (29)$$

$$\text{where } V_c = SquaredReLU(K_c) \quad (30)$$

### 7.3. Bilateral Spectrum Aligner Block

This subsection focuses on the three core components of the Bilateral Spectrum Aligner: Spectral Alignment Enhancer (SAE), Cross Attention (CA), and Scharr Edge Enhancement (SEE).

#### 7.3.1 Spectral Alignment Enhancer (SAE)

To enhance the low-light image enhancement model's perception and processing of spectral features under varying illumination conditions, we propose an adaptive feature-enhancement module termed the Spectral Alignment Enhancer (SAE), illustrated in Figure 6. Specifically, the module achieves precise optimization of low-light features through three sequential stages: feature expansion, separated enhancement, and interactive fusion.

Initially, the input feature  $F \in \mathbb{R}^{C \times H \times W}$  is channel-wise expanded via a  $1 \times 1$  convolution and then split into

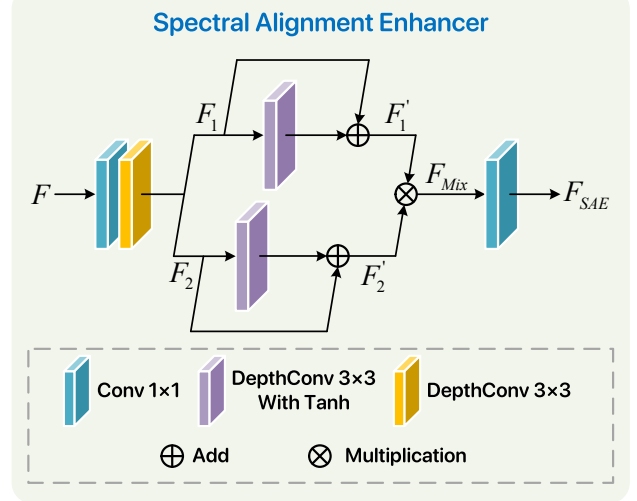


Figure 6. Spectral Alignment Enhancer's structure.

two branches, thereby preserving sufficient expressive capacity for capturing faint spectral details in low-light environments.

$$F_1, F_2 = Split(DepthConv_{3 \times 3}(Conv_{1 \times 1}(F))) \quad (31)$$

Here,  $Split(\cdot)$  denotes an even channel-wise halving.

Subsequently, the two feature streams  $F_1, F_2 \in \mathbb{R}^{C_{1/2} \times H \times W}$  are each processed by a depthwise-separable convolution to focus on local spatial patterns, followed by a nonlinear Tanh activation and a residual connection, resulting in refined features  $F'_1, F'_2 \in \mathbb{R}^{C_{1/2} \times H \times W}$ . This design allows the SAE to enhance the extraction of critical low-light cues, such as edges and textures, while preventing detail loss caused by excessive transformations. The procedure can be expressed as:

$$F'_1 = F_1 + Tanh(DepthConv_{3 \times 3}(F_1)) \quad (32)$$

$$F'_2 = F_2 + Tanh(DepthConv_{3 \times 3}(F_2)) \quad (33)$$

Finally, the two refined feature streams are multiplied element-wise to achieve dynamic interaction, adaptively reinforcing informative cues. A subsequent  $1 \times 1$  convolution then compresses the result back to the original channel dimension, yielding the optimized feature  $F_{SAE} \in \mathbb{R}^{C \times H \times W}$ . This process is formulated as:

$$F_{SAE} = Conv_{1 \times 1}(F'_1 \times F'_2) \quad (34)$$

#### 7.3.2 Cross Attention (CA)

In low-light enhancement, the luminance stream  $x$  and the chrominance stream  $y$  are usually mis-aligned in both spatial statistics and semantic content. We propose a lightweight Cross-Attention (CA) block that lets  $x$  query

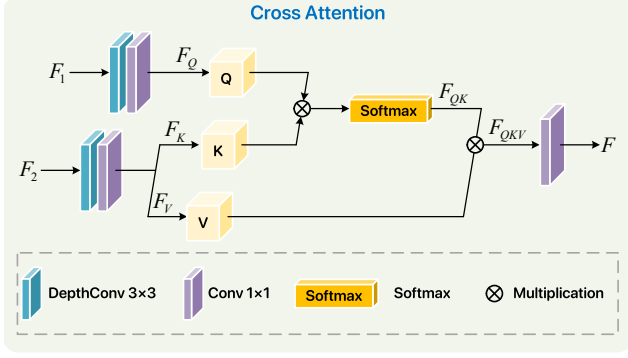


Figure 7. Cross Attention's structure.

relevant information from  $y$  through a multi-head, L2-normalized cross-covariance attention implemented with depth-wise convolutions only. The entire procedure is summarized below with strict correspondence to the released code, illustrated in Figure 7.

First, Given two feature maps:

$$x, y \in R^{C \times H \times W} \quad (35)$$

, where  $x$  originates from the brightness subnet and  $y$  from the color subnet.

Query / Key / Value Generation

All linear projections are instantiated as  $1 \times 1$  convolutions followed by  $3 \times 3$  depth-wise convolutions to retain local context while being parameter-efficient.

$$Q = DWConv_{3 \times 3}(Conv_{1 \times 1}(x)) \in R^{C \times H \times W} \quad (36)$$

$$KV = DWConv_{3 \times 3}(Conv_{1 \times 1}(y)) \in R^{2C \times H \times W} \quad (37)$$

The KV tensor is then channel-split into key and value:

$$K, V = split(KV, dim = 1), K, V \in R^{C \times H \times W} \quad (38)$$

Multi-Head Re-Shape and L2-Normalization

To exploit complementary attention patterns, we reshape each tensor into  $h$  heads:

$$Q_{head} = rearrange(Q) \in R^{n_h \times c_h \times (H \cdot W)} \quad (39)$$

$$K_{head} = rearrange(K) \in R^{n_h \times c_h \times (H \cdot W)} \quad (40)$$

$$V_{head} = rearrange(V) \in R^{n_h \times c_h \times (H \cdot W)} \quad (41)$$

To ensure training stability, L2-normalization is applied along the last dimension:

$$\hat{Q} = \frac{Q_{head}}{\|Q_{head}\|_2}, \hat{K} = \frac{K_{head}}{\|K_{head}\|_2} \quad (42)$$

Cross-Covariance Attention

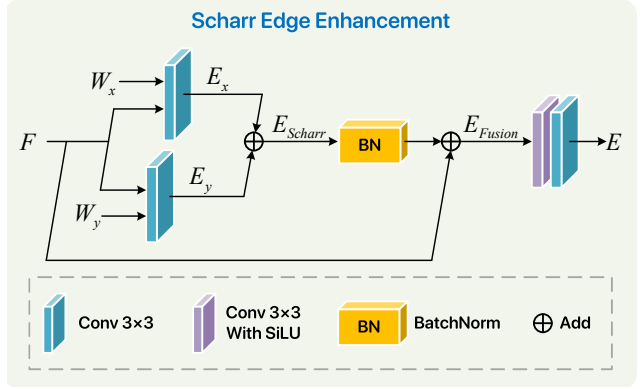


Figure 8. Scharr Edge Enhancement's structure.

We compute the cross-covariance attention matrix between  $x$ -query and  $y$ -key:

$$attn = softmax\left(\frac{\hat{Q}\hat{K}^T}{\tau}\right) \in R^{n_h \times c_h \times c_h} \quad (43)$$

where the temperature  $\tau$  is a learnable scalar initialized to 1. The attended feature is then aggregated via matrix multiplication with  $y$ -value:

$$out = attn \cdot V_{head} \in R^{n_h \times c_h \times (H \cdot W)} \quad (44)$$

Output Projection

Finally, the multi-head output is re-arranged and projected back to the original channel dimension via a  $1 \times 1$  convolution:

$$Output = Conv_{1 \times 1}(rearrange(out)) \in R^{C \times H \times W} \quad (45)$$

The resulting tensor is element-wise added to the luminance branch, yielding an enhanced feature that is both color-aware and noise-suppressed.

### 7.3.3 Scharr Edge Enhancement (SEE)

In the field of low-light image enhancement, the accurate preservation of edge contours and the complete recovery of texture details have always been core challenges that restrict the performance of algorithms. In low-light environments, the image Signal-to-Noise Ratio (PSNR) decreases significantly, causing the gradient information in edge regions to be submerged by noise and thus become weak. Meanwhile, traditional enhancement methods, in the process of improving brightness, often further exacerbate edge blurring and texture loss due to excessive smoothing operations or noise amplification effects, ultimately leading to visual distortion in the enhanced results characterized by "improved brightness but lacking details", illustrated in Figure 8.

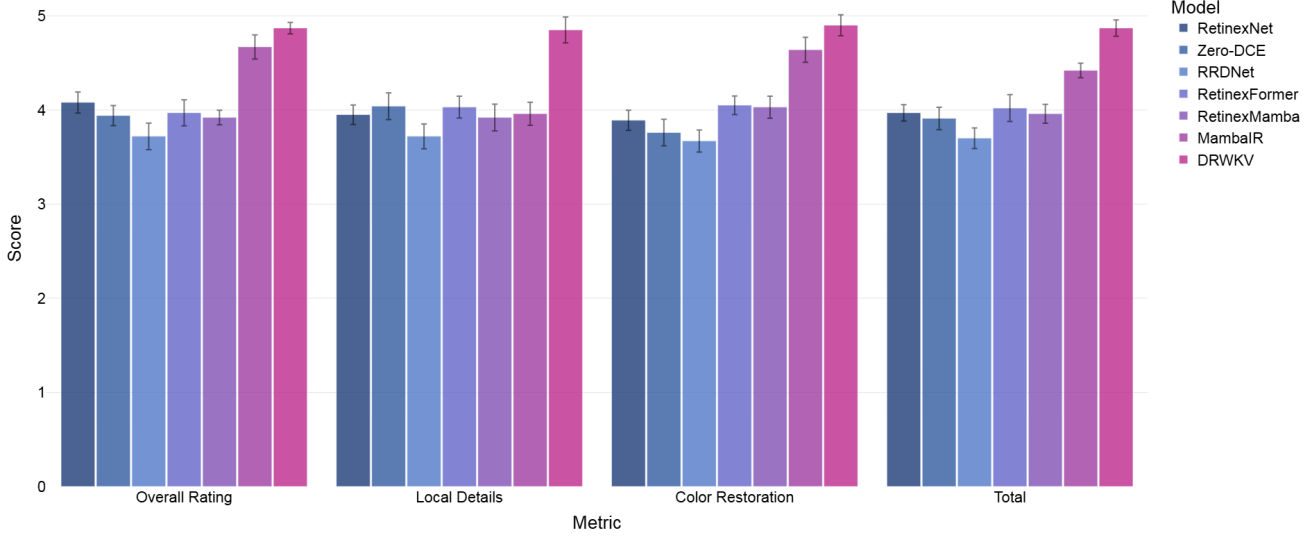


Figure 9. User subjective evaluation experiment.

#### 7.4. User Subjective Evaluation Experiment

To address the above issues, we propose a Scharr Edge Enhancement (SEE) module. By integrating the prior knowledge of traditional image processing with the feature learning capability of deep learning, it provides an effective solution for structure-aware enhancement in low-light scenarios. Specifically, given the input feature  $F \in \mathbb{R}^{C \times H \times W}$ , we first perform channel-wise filtering operations using pre-fixed Scharr convolution kernels and convolution weights  $W_x, W_y$  to simulate the gradient extraction process in traditional image processing, obtaining the x-direction gradient feature  $E_x \in \mathbb{R}^{C \times H \times W}$  and y-direction gradient feature  $E_y \in \mathbb{R}^{C \times H \times W}$  respectively.

Subsequently, to suppress noise interference and aggregate multi-directional edge information, we fuse  $E_x$  and  $E_y$  using the L1 norm to compute the Scharr edge strength feature  $E_{Scharr} \in \mathbb{R}^{C \times H \times W}$ .

Then, the edge strength feature is integrated with the original input feature through a residual mechanism to obtain the fused feature  $E_{Fusion} \in \mathbb{R}^{C \times H \times W}$ . This operation, on one hand, preserves the structural prior in the original feature; on the other hand, it avoids "edge overexposure" caused by excessive feature transformation under the guidance of edge information, thereby ensuring the naturalness of edge enhancement.

Finally, to achieve adaptive adjustment of feature dimensions and deep fusion of semantic information,  $1 \times 1$  convolution and  $3 \times 3$  convolution are used for dimension reduction and recovery, resulting in the final output  $SEE_{out} \in \mathbb{R}^{C \times H \times W}$ .

The specific calculation process can be expressed as fol-

lows:

$$E_x = Conv_{3 \times 3}(F, W_x), E_y = Conv_{3 \times 3}(F, W_y) \quad (46)$$

$$W_x = \begin{bmatrix} -3 & 0 & 3 \\ -10 & 0 & 10 \\ -3 & 0 & 3 \end{bmatrix}, W_y = \begin{bmatrix} -3 & -10 & -3 \\ 0 & 0 & 0 \\ 3 & 10 & 3 \end{bmatrix} \quad (47)$$

$$E_{Scharr} = \|E_x\|_1 + \|E_y\|_1 \quad (48)$$

$$E_{Fusion} = F + BN(E_{Scharr}) \quad (49)$$

$$SEE_{out} = Conv_{3 \times 3}(SiLU(Conv_{1 \times 1}(E_{Fusion}))) \quad (50)$$

Here,  $Conv_{3 \times 3}(\cdot, \cdot)$  denotes a  $3 \times 3$  convolution with fixed weights,  $BN(\cdot)$  represents the BatchNorm operation, and  $SiLU(\cdot)$  denotes the SiLU activation function.

#### 8. The input of the Global Edge Retinex theory

In the main text, we elaborate and derive the proposed GER, and present the input structure in the main text figures: edge features  $E$ , artifacts  $S$ , and processed global illumination  $L_{ill}$ . As the artifacts  $S$  and processed global illumination  $L_{ill}$  have been thoroughly explained, in the appendix, we discuss the extraction and integration of edge features  $E$ .

To reduce the computational load and complexity of the model itself, we further utilize the SEE based on the output  $I_{DRWKV} \in \mathbb{R}^{3 \times H \times W}$  of the DRWKV model, thereby obtaining the integration of input edge features  $E$  suitable for Global Edge Retinex theory.

The specific calculation process can be expressed as follows:

$$E = SEE(I_{DRWKV}) \quad (51)$$

## 9. Extended experiment

### 9.1. User Subjective Evaluation Experiment

To rigorously assess the perceptual quality of enhancement algorithms under complex real world conditions we designed and conducted a user subjective evaluation experiment. Ten low light images were randomly selected from the publicly available LSRW Huawei benchmark and processed by seven enhancement models: RetinexNet, ZeroDCE, RRDNet, RetinexFormer, RetinexMamba, MambaIR and the proposed DRWKV to generate corresponding enhanced results. One hundred participants spanning diverse ages and professional backgrounds were then recruited. In an independent double blind protocol participants assigned scores on a five point Likert scale from one worst to five best along three key perceptual dimensions overall visual quality local detail restoration and global color fidelity. The mean opinion scores are reported in Figure 9. Across all three dimensions the proposed DRWKV model achieved the highest ratings indicating superior perceptual enhancement performance from the human visual perspective.

### 9.2. Low-light Object Tracking Experiment

The aforementioned experiments have demonstrated that DRWKV already exhibits superior performance in basic experimental scenarios. To investigate its generalization ability, we designed a low-light multi-object tracking task. For the dataset, we adopted the Drone low-light tracking benchmark, UAVDark135. It contains 135 video sequences in total, encompassing various tracking scenarios such as intersections and highways, as well as tracking targets including pedestrians, boats, and vehicles. The videos are captured at a frame rate of 30 FPS with a resolution of 1920×1080.

In terms of methodology, we compared the performance of mainstream object tracking algorithms with and without the integration of the DRWKV low-light enhancement module, using MOTA (multi-object tracking accuracy), IDF1 (identity recognition F1 score), and HOTA (high-order tracking accuracy) as evaluation metrics.

The experimental conclusions show that DRWKV generally improved accuracy across multiple mainstream tracking algorithms, with particularly prominent performance in multi-object tracking and identity preservation. Meanwhile, the limitations of this module in optimizing Deep OC-SORT warn us that in the face of low adaptability and weak tuning of network structures, it may not be possible to achieve simultaneous improvements in detection accuracy and association capability.

### 9.3. $\alpha$ , $\beta$ and $\gamma$ Parameter Detail Experiment

To obtain the optimal configuration of the three parameters ( $\alpha$ ,  $\beta$  and  $\gamma$ ), we designed a series of parameter detail experiments. For the dataset, we adopted the LOLv2-Real

dataset. During the implementation of the parameter detail experiments, we only adjusted one of the three parameters ( $\alpha$ ,  $\beta$  and  $\gamma$ ) while keeping the other two unchanged. The experimental results are presented in Table 5, Table 6, and Table 7. These results indicate that the optimal parameter configuration for DRWKV is  $\alpha = 0.2$ ,  $\beta = -0.05$ , and  $\gamma = 0.2$ .

Table 5. The impact of different  $\alpha$  values on the performance of the LOLv2-Real dataset.

$\alpha$	0.05	0.10	0.15	<b>0.20</b>	0.25	0.30	0.35
PSNR $\uparrow$	23.56	23.89	24.02	<b>24.12</b>	23.84	23.97	23.94
SSIM $\uparrow$	0.798	0.815	0.814	<b>0.832</b>	0.792	0.821	0.814
NIQE $\downarrow$	4.012	3.967	3.941	<b>3.926</b>	3.951	3.989	4.173

Table 6. The impact of different  $\beta$  values on the performance of the LOLv2-Real dataset.

$\beta$	-0.100	-0.075	<b>-0.050</b>	-0.025	0
PSNR $\uparrow$	23.72	23.98	<b>24.12</b>	23.86	23.61
SSIM $\uparrow$	0.803	0.821	<b>0.832</b>	0.817	0.804
NIQE $\downarrow$	3.995	3.948	<b>3.926</b>	3.973	4.003

Table 7. The impact of different  $\gamma$  values on the performance of the LOLv2-Real dataset.

$\gamma$	0.05	0.10	0.15	<b>0.20</b>	0.25	0.30	0.35
PSNR $\uparrow$	22.74	23.65	23.91	<b>24.12</b>	23.99	23.78	23.84
SSIM $\uparrow$	0.804	0.801	0.823	<b>0.832</b>	0.826	0.812	0.814
NIQE $\downarrow$	4.112	4.023	3.957	<b>3.926</b>	3.962	3.998	4.472